

245 A REMOTE MICROPHYSICAL STUDY OF SEVERE WIND-PRODUCING CONVECTIVE STORMS

Kenneth L. Pryor
Center for Satellite Applications and Research (NOAA/NESDIS)
College Park, MD

1. INTRODUCTION AND BACKGROUND

Convective storms that generate hail, lightning, and damaging winds have been identified as a formidable hazard to life and property. Even more impactful are stronger storms that generate and loft liquid-phase hydrometeors to high altitudes where freezing occurs and collisions between drops, graupel, and ice crystals lead to electrification. Condensate loading, sometimes combined with the lateral entrainment of subsaturated air in the storm middle level, initiates the convective downdraft. The subsequent melting of frozen hydrometeors and subcloud evaporation of liquid precipitation, in conjunction with precipitation loading, result in the cooling and negative buoyancy that accelerate the downdraft in the unsaturated layer. A downburst, in general, is defined as a strong downdraft that induces an outburst of damaging winds at or near the ground, and a microburst as a very small downburst with an outflow diameter of less than 4 km and a lifetime of less than 5 minutes (Fujita 1985; Wakimoto 1985). Previous studies of the microphysical structure of downburst-producing convective storms have entailed analysis of polar and geostationary satellite imagery and derived products, meteorological Doppler radar, and in-situ surface wind observations. The current study expands upon previous analysis by incorporating lower tropospheric vertical wind and temperature profile data generated by the Cooperative Agency Profilers (CAP) system that consists of Boundary Layer Profiler (BLP) instruments, operating at a frequency of 915 MHz, and Radio Acoustic Sounding System (RASS) instruments. In addition, Geostationary Lightning Mapper (GLM) data from Geostationary Operational Environmental Satellite (GOES)-16 will also be displayed and analyzed to better explain the role of lightning in a downburst-producing convective storm.

Among the most widely accepted theories of convective storm electrification is the “charge transfer-separation process” by which interaction (esp. collision) between ice crystals and graupel particles result in the establishment and stratification of positive and negative charge centers within the convective cloud, respectively. Differing growth processes between ice crystals (i.e. deposition of water vapor) and graupel (accretion of supercooled water) result in differing molecular structure and electron arrangement, and subsequently, favor the transfer of electrons with negative charge from an ice crystal to a graupel particle. In general, negative charge accumulates in the middle levels of the convective storm cloud, referred to as the “main negative charge” center, while positive charge accumulates in the upper layer and anvil (if present) region and is referred to as the “upper positive charge” center (Krehbiel 1983). Other secondary charge centers may develop in a convective storm, such as the “lower positive charge” center that results from falling hail, however, the main electric field built within the storm results from the separation of the main negative and upper positive charge centers. When the electric field strength (E) between the storm cloud and the ground eventually increases to the threshold value of electric breakdown potential (3×10^9 V/km, Stull (2017)), a stepped leader, defined as a segmented ionized channel, develops and propagates downward toward the ground in steps of 50 to 100 m length (Holle and Lopez 1993). Upon contact of the stepped leader with the ground, a bright return stroke from the ground to the cloud occurs, in which electrons flow downward from progressively higher levels in the channel. The stepped leader and return stroke comprise the lightning strike. The strike with additional return strokes, triggered by a dart leader, then comprise the cloud-to-ground (CG) lightning flash. Intracloud (IC) lightning discharge between the main negative and upper positive charge centers also results from charge separation and electrical breakdown. Ground-based and satellite-based lightning detection systems often detect both IC and CG lightning flashes, with CG strokes a stronger emitter of low frequency (LF) radiation.

*Corresponding author address: Kenneth L. Pryor, NOAA/NESDIS/STAR, 5830 University Research Ct., College Park, MD 20740; e-mail: Ken.Pryor@noaa.gov.

Lightning detection systems (LDS) have a vital role in the real-time identification of the location of lightning strokes for the purpose of public safety and weather forecasting and warning operations. Archived LDS datasets also provide support to electric utility companies to identify lightning events associated with electric power grid faults and power outages, reduce frequency and duration of power outages, and make improvements to transmission line segments susceptible to lightning damage (Murphy 2018). More importantly, flash rate and density measurements are necessary for the inference of cloud thermodynamical and microphysical processes that favor severe thunderstorm hazard phenomena including hail, tornadoes, and damaging winds (downbursts).

Selected thunderstorm events that demonstrate the physical process of downburst generation as observed simultaneously by the GOES-16 Advanced Baseline Imager (ABI) and GLM, Doppler radar (NEXRAD), and boundary layer profilers will be analyzed in this paper. Vertical sounding profile data from the CAP system has been applied as a supplement to Sounding/Hodograph Analysis and Research Program in Python (SHARPPy)-generated thermodynamic profiles to further study the favorable environment for severe convective storm winds. On the afternoon of 1 August 2017, severe downburst-producing thunderstorms occurred in the United States Mid-Atlantic region and over southern California that resulted in tree damage, downed power lines, and traffic disruptions. As shown later in this paper, for both of these events, GOES-16 ABI split window (channel 15 – 13) brightness temperature difference (BTD) imagery (Inoue 1987) at 2-km resolution displayed a high level of detail in storm structure and was effective in identifying storm-scale features, including cold cloud tops and dry-air intrusions. Corresponding GLM imagery displayed clusters of lightning flashes in close proximity to downburst events near the time of occurrence.

2. PHYSICAL CONCEPTS OF LIGHTNING DETECTION

Two distinct types of lightning detection systems are being considered for this review: ground-based (low frequency) and satellite-based (optical transient detector). Ground-based systems employ an array of sensors that receive radiofrequency (RF) emissions in the form of electromagnetic waves (sferics) at low

frequencies, typically below 500 kHz, and use either direction-finding or time-of-arrival (TOA) methods for lightning strike location. Very low frequency (VLF) detectors are highly favorable for long distance lightning emissions in which VLF waves are trapped in a waveguide between the ionosphere and the ground. The Washington, DC Lightning Mapping Array (DCLMA, available online at <https://lightning.nsstc.nasa.gov/lma/dclma/dclma.shtml#>) locates the total lightning activity using a network of ten stations applying the TOA method to 60 MHz RF radiation from lightning discharges. The TOA method is graphically described in Figure 1. For a given time-of-arrival difference, the stroke that emitted the signal could be located anywhere along one of the branches of a hyperbola passing between the two receivers that are foci points of that hyperbola (Holle and Lopez 1993). The intersection of two non-redundant hyperbola branches defines the location of the stroke at the open circle in Figure 1.

The Geostationary Operational Environmental Satellite (GOES)-16 Geostationary Lightning Mapper (GLM) is a high speed event detector operating in the near infrared portion of the electromagnetic spectrum with a wide field-of-view (FOV) lens combined with a narrow-band interference filter focused on a high speed Charge Coupled Device (CCD) focal plane (Goodman et al. 2013). The GLM operates at 0.78 μm wavelength with a sub-point resolution of 8 km and a temporal resolution of 20 seconds. The GLM produces total lightning (IC + CG) over a location of interest with active convective storms in progress. The Lightning Cluster Filter Algorithm (LCFA), graphically described in Figure 2, performs temporal-spatial clustering of lightning event data into groups and flashes which can then be used to locate the initiation, propagation and horizontal extent of an individual flash within the GLM field of view.

3. METHODOLOGY

Selected thunderstorm events that demonstrate the physical process of downburst generation as observed simultaneously by the Geostationary Operational Environmental Satellite (GOES)-16 Advanced Baseline Imager (ABI) and Geostationary Lightning Mapper (GLM), Doppler radar (NEXRAD), the Washington, DC Lightning Mapping Array (DCLMA, available online at <https://lightning.nsstc.nasa.gov/lma/dclma/dclma.shtml#>) and boundary layer profilers (BLP) are

analyzed. Data collection, processing, and visualization for this study follow the methodology of Pryor (2015, 2017). GOES-16 product images were generated by Python programs where GOES imager ABI brightness temperature data was read and processed, and output BTD values were mapped using the Python 2D plotting library (Matplotlib, <https://matplotlib.org/>). The image data consisted of derived brightness temperatures from ABI infrared bands 13 and 15, obtained from the NESDIS/STAR Central Data Repository (SCDR). The RAOB thermodynamic profiles shown in Figure 2 were generated by the Sounding/Hodograph Analysis and Research Program in Python (SHARPPy, <https://github.com/sharppy/SHARPPy>). SHARPPy is a collection of open source sounding and hodograph analysis routines. NEXRAD PPI and vertical cross section images were generated by Python programs employing the Python ARM Radar Toolkit (Py-ART, <http://arm-doe.github.io/pyart/dev/index.html>). Vertical temperature and wind profile data, up to 5 km AGL, from the Cooperative Agency Profilers (CAP) system has been applied to further study the favorable environment for severe convective storm winds.

The Next Generation Weather Radar (NEXRAD) level-II reflectivity and differential reflectivity factor ZDR were obtained from the National Climatic Data Center (NCDC) and used to verify that observed wind gusts were associated with downbursts originating from high reflectivity factor storms and were not associated with other types of convective wind phenomena (i.e., gust fronts). Plan-view images of radar reflectivity and ZDR were constructed from the lowest elevation angle scan (0.46°). An additional application of radar reflectivity factor imagery is to infer microscale physical properties of downburst-producing convective storms. Differential reflectivity factor was employed in the case studies in this paper to analyze the vertical precipitation composition in convective storms and thereby indicate the presence of graupel and hail and discuss their role in the enhancement of convective downdrafts. A particular reflectivity signature, the protrusion echo (Knupp 1996), is an effective indicator of the occurrence of downbursts and was identified in this study to indicate downburst occurrence. Downburst occurrence was further confirmed by calculating a surface ΔT value, where $\Delta T \equiv T(\text{downburst}) - T(\text{ambient})$ and represents the peak temperature departure from ambient at ground level (Proctor 1989). ΔT can therefore serve as a proxy variable

for the surface density perturbation through the ideal gas law.

4. CASE STUDIES

4.1 1 August 2017 Downbursts: Frederick, Maryland

During the afternoon of 1 August 2017, a cluster of strong thunderstorms developed and tracked southward in a convectively unstable air mass over the Blue Ridge Mountains of Maryland. A particularly intense thunderstorm cell developed on the southern end of the cluster and produced a severe downburst in Frederick, Maryland near 1800 UTC (1400 EDT). Wind damage resulting from the downburst included damaged trees, power lines, and utility poles, and resulted in over 3,000 Potomac Edison customers losing electricity. The RAP model thermodynamic profile in Figure 3 over Frederick (FDK) indicates favorable atmospheric conditions for strong convective storms and intense downdraft development, including large CAPE ($> 1500 \text{ J kg}^{-1}$), and a 200 mb deep unsaturated layer centered at the 500 mb level, overlying a surface-based convective mixed layer with a near dry-adiabatic lapse rate. Figures 4 and 5 display GOES-16 split-window BTD image products between 1800 and 1805 UTC, near the time of downburst occurrence, that show prominent dry-air notches evolving on the eastern to southern flanks of the storm, and the appearance of an overshooting top (BTD $> -1^\circ\text{C}$, white shading) that signified maximum updraft intensity. The appearance of these features in GOES imagery corresponded to the appearance and evolution of inflow notches in NEXRAD reflectivity imagery in Figures 6 to 8, and an increase in reflectivity nearly overhead the location of downburst impact. Inflow notch development most likely indicated the simultaneous occurrence of lateral entrainment and wake entrainment (Knupp 1989) on the downshear flank of the storm which have been identified as a typical and salient forcing mechanisms for intense downdrafts. Even more importantly, protrusion echoes ("PE") were prominent during the ten-minute period of downburst occurrence. Increasing differential reflectivity (ZDR) values from 1 to 4, also shown in Figures 6 to 8, indicated the melting of hail and subsequent increase in raindrop size near the ground as storm outflow intensified. Near the end of the downburst event, at 1809 UTC, the collection of large raindrops by the burst front was apparent as a localized linear region of high ZDR

values (red shading) on the southeastern flank of the thunderstorm. In addition, the ΔT value computed for this event of -11 to -12 °C is consistent with a wet microburst associated with a hail-producing thunderstorm (Figure 20, Proctor 1989). GOES-16 imagery at 2-km resolution displayed a higher level of detail in storm structure as compared to GOES-13 imagery (not shown) at 4-km resolution, and was effective in identifying storm-scale features as compared to NEXRAD imagery. The inflow notch in radar imagery is a signature associated with downburst generation, and the resulting downburst wind damage.

Vertical cross sections of NEXRAD reflectivity and differential reflectivity in Figures 9 and 10 reveal important features pertaining to storm structure and the favorability for downbursts. The development of a layer of graupel above the freezing level during the late towering cumulus stage and early mature stage of the thunderstorm likely resulted in cloud electrification. In addition, the graupel, detected in the storm regions with low ZDR (-1 to +1 dB, green shading) and co-located moderate reflectivity (30 – 50 dBZ), served as hail embryos, and contributed to subsequent downdraft initiation. The descending core of low ZDR values, collocated with high reflectivity (> 50 dBZ), signified the presence of a descending hail shaft that fostered an intense downdraft due to the combined effects of precipitation loading and melting of ice. Descent of the hail shaft below the melting level between 1801 and 1805 UTC marked the onset of the downburst. During this time, GOES-16 GLM LCFA imagery indicated a slight decrease in flash rate and a concentration of lightning events on the southeastern (downwind) flank of the storm. Accordingly, concurrent DCLMA imagery in Figure 14 shows a spatial pattern of lightning RF emissions similar to the spatial pattern of the storm as shown in radar reflectivity imagery, with the most powerful emissions clustered near the location of downburst occurrence.

During the late afternoon of 1 August, a line of thunderstorms developed between the Washington, DC and Baltimore, Maryland metropolitan areas. As shown in Figure 11, the southernmost storm of the line intensified over Washington, DC and evolved into a bow echo as the storm tracked northeastward into Montgomery and Prince Georges counties in Maryland during the early evening. Similar to the Frederick downburst earlier in the afternoon, cross section imagery in Figure 12 indicates the

presence of a hail core descending below the melting level. Between 2230 and 2240 UTC, this thunderstorm produced a low-end downburst with a wind gust of 20 kt (from a north-northeasterly direction) recorded in Riverdale. The Beltsville BLP captured the passage of this outflow boundary that was characterized by an abrupt wind shift and increasing wind speed through a deepening surface-based layer, as shown in Figure 13. The 20-kt wind speed recorded by the profiler between 2248 and 2254 UTC, below a height of 500 m, corresponded to the wind gust speed measured in Riverdale, and was from the opposite direction (south-southwest), suggesting that this outflow originated from the same storm about 12 km southwest of the station.

4.2 1 August 2017 Downbursts: San Diego, California

During the afternoon of 1 August 2017, a cluster of strong thunderstorms developed along the eastern boundary of the southern California marine layer and tracked northwestward over the foothills of the Laguna Mountains in San Diego County. A particularly intense thunderstorm cell developed east of San Diego and produced small hail and a strong downburst between 2020 and 2030 UTC that resulted in downed trees and traffic disruptions in the Alpine area.

The Rapid Refresh (RAP) model-derived vertical sounding profile over San Diego (NKX) in Figure 3 near the time of downburst occurrence (2100 UTC) indicates conditions favorable for strong outflow wind-producing thunderstorms that included the presence of an elevated mixed layer and resulting inflow of sub-saturated air into the thunderstorm cloud base. Figures 15 and 16 display GOES-16 split-window BTD image products between 2025 and 2030 UTC, near the time of downburst occurrence, that showed a prominent dry-air notch evolving on the eastern flank of the storm signifying the contribution of lateral entrainment to downdraft initiation. During this time, GOES-16 GLM LCFA imagery indicated a slight increase in flash rate and a concentration of lightning events on the eastern (upwind) flank of the storm. NEXRAD reflectivity imagery in Figures 17 and 18 show a prominent dry-air/inflow notch and protrusion echo on the southeastern flank of the storm near the time of downburst occurrence. Similar to the Frederick downburst, the protrusion echo, frequently associated with a bow echo, indicates a high likelihood of downburst generation. ZDR imagery in Figure 18 as well as vertical cross sections of

reflectivity and ZDR in Figures 19 and 20 effectively display the evolution of the burst front on the eastern flank of the storm, as a localized region of high ZDR values and a “foot”-shaped appendage in reflectivity imagery. Reflectivity cross section imagery in Figures 19 and 20 exhibits similar structural characteristics to the Frederick storm, with a well-defined hail shaft descending below the melting level and graupel layer. The production of hail and contribution of hail to downburst intensity was confirmed by the observation of pea-sized (6-7 mm) hail on the ground at Alpine. Goodman et al. (1988) identified the mixture of rain and pea-sized hail as a precursor to microburst onset at the surface. Between 2020 and 2030 UTC, downburst wind gusts of 35 to 40 knots were recorded by mesonet stations in Alpine and West Alpine, respectively. The ΔT value computed for this event of -11 to -12 °C was again consistent with a hail-producing, thunderstorm-generated downburst.

5. DISCUSSION AND CONCLUSION

Ground based lightning detection systems, especially the DCLMA, that are also covered by satellite-based detection systems, such as the GOES-16 GLM, can provide a more comprehensive physical model for severe thunderstorm generation and associated hazards including hail and damaging wind. For the severe downburst event that occurred in Frederick on 1 August 2017, DCLMA and GLM LFCA datasets were compared with GOES-16 ABI and Doppler radar reflectivity data to infer patterns of lightning flash density just prior to downburst occurrence. GOES-16 ABI split window channel BTD imagery at 2-km resolution displayed a high level of detail in storm structure and was effective in identifying storm-scale features, including cold cloud tops and dry-air intrusions. Corresponding GLM imagery displayed lightning events in close proximity to downburst events at the time of downburst occurrence. Interestingly, GLM LFCA output over a one minute period (1805-1806 UTC) near the time of downburst occurrence shows an increased concentration of flash activity on the southeastern flank of the storm, while lightning events propagated with storm motion toward the southeast. A similar trend is noted in concurrent DCLMA imagery in Figure 14, where maxima in RF source emissions propagate in the direction of storm motion in close proximity to downburst occurrence. Satellite-based lightning detection methods indicate an eastward displacement of maximum flash density away

from the location of downburst impact at both Frederick and Alpine which suggests that storm structure (i.e. storm tilt and anvil development relative to the main precipitation core) influences spatial patterns of lightning occurrence. More importantly, the presence of mixed phase precipitation (supercooled water, graupel, hail, ice crystals) that favors storm electrification also favors intense downdraft development due to loading, melting and evaporational cooling effects. In summary, the building of an electric field within the storm also generates downdraft potential energy that is eventually realized as kinetic energy resulting from evaporation of water and melting of graupel and hail.

6. REFERENCES

- Ellrod, G. P., and K. Pryor, 2018: Applications of Geostationary Satellite Data to Aviation. *Pure and Applied Geophysics*, 1-27. <https://doi.org/10.1007/s00024-018-1821-1>
- Fujita, T.T., 1985: The downburst, microburst and macroburst. Satellite and Mesometeorology Research Paper 210, University of Chicago, 122 pp.
- Goodman, S.J., D.E. Buechler, P.D. Wright, and W.D. Rust, 1988: Lightning and precipitation history of a microburst-producing storm. *Geophys. Res. Lett.*, **15**, 1185-1188.
- Goodman, S. J., Blakeslee, R. J., Koshak, W. J., Mach, D., Bailey, J., Buechler, D., 2013: The GOES-R Geostationary Lightning Mapper (GLM). *Atmospheric Research*, **125–126**, 34–49.
- Holle, R. L., and P.E. Lopez, 1993: Overview of real-time lightning detection systems and their meteorological uses. NOAA Technical memorandum ERL NSSL-102. National Severe Storms Laboratory, Norman, OK, 68 pp.
- Inoue, T., 1987: A cloud type classification with NOAA 7 split-window measurements. *Journal of Geophysical Research: Atmospheres*, **92(D4)**, 3991-4000.
- Knupp, K. R., 1989: Numerical simulation of low-level downdraft initiation within precipitating cumulonimbi: Some preliminary results. *Mon. Wea. Rev.*, **117**, 1517–1529, doi:10.1175/1520-0493(1989)117,1517:NSOLLD.2.0.CO;2.
- Knupp, K. R., 1996: Structure and evolution of a long-lived, microburst producing storm. *Mon. Wea. Rev.*, **124**, 2785–2806, doi:10.1175/1520-0493(1996)124,2785:SAEOAL.2.0.CO;2.
- Krehbiel, P.R., 1986: The electrical structure of thunderstorms, The Earth's Electrical Environment. E.P. Krider and R.G. Roble, eds 95 pp.
- Murphy, M., 2018: Locating Lightning. *Physics Today*, **71(3)**, 32-38.
- National Weather Service Training Center, cited 2018: Operational Uses of Lightning Data. https://training.weather.gov/nwstc/METEOR/Lighting/Ltng_home.htm
- Proctor, F.H., 1989: Numerical simulations of an isolated microburst. Part II: Sensitivity experiments. *J. Atmos. Sci.*, **46**, 2143-2165, doi: 10.1175/1520-0469(1989)046<2143:NSOAIM>2.0.CO;2
- Pryor, K. L., 2015: Progress and Developments of Downburst Prediction Applications of GOES. *Wea. Forecasting*, **30**, 1182–1200, doi: 10.1175/WAF-D-14-00106.1.
- Pryor, K. L., 2017: Advances in downburst monitoring and prediction with GOES-16. Proc. 17th conf. on mesoscale processes, San Diego, CA, Amer. Meteor. Soc., Paper (No. 10.6).
- Stull, R., 2017: "Practical Meteorology: An Algebra-based Survey of Atmospheric Science" - version 1.02b. Univ. of British Columbia. 940 pages.
- Wakimoto, R. M., 1985: Forecasting dry microburst activity over the high plains. *Mon. Wea. Rev.*, **113**, 1131–1143, doi:10.1175/1520-0493(1985)113,1131:FDMAOT.2.0.CO;2.

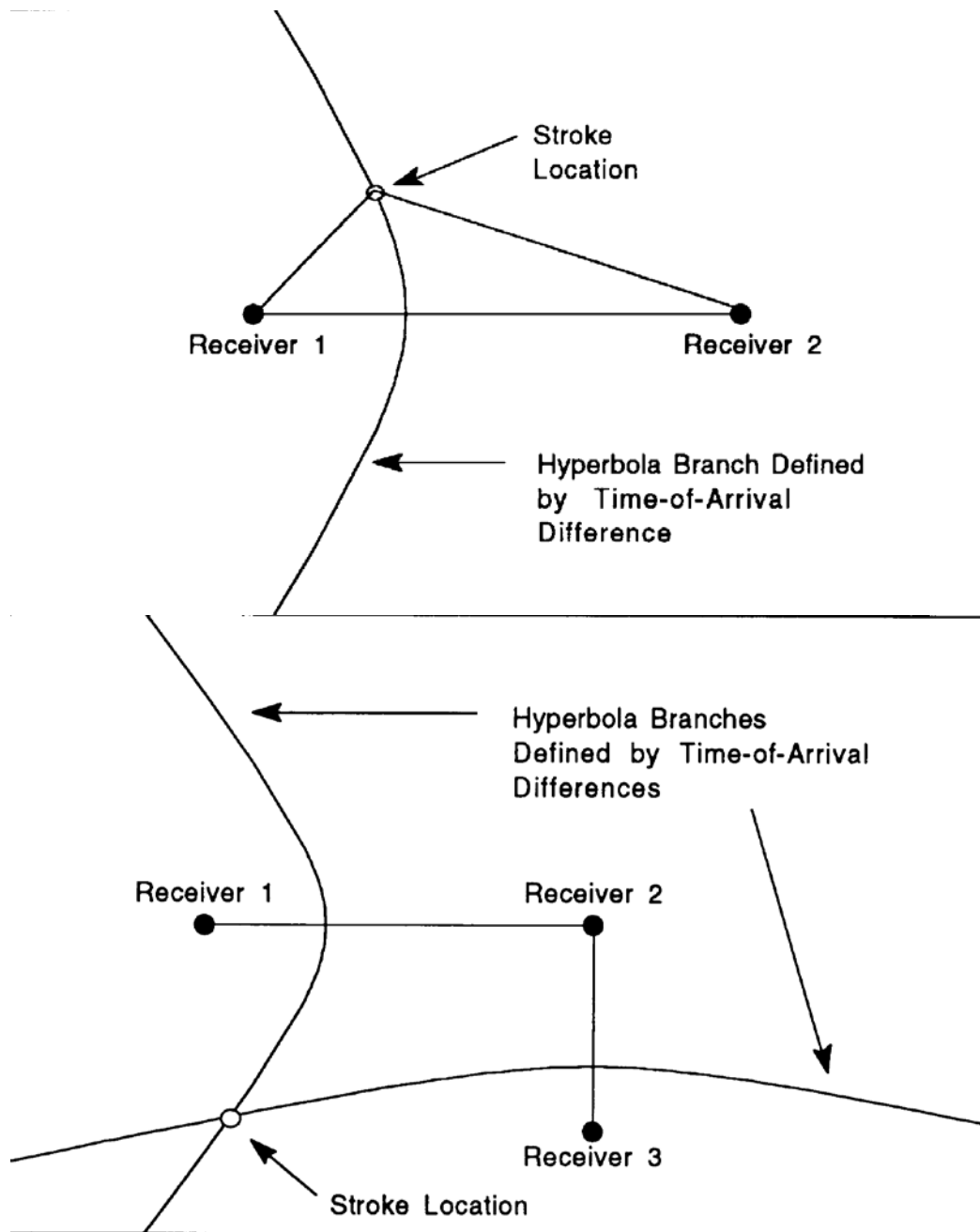


Figure 1. Graphical description of the time-of-arrival method of lightning location that is employed by ground-based systems such as the DCLMA. For a given time-of-arrival difference, the stroke that emitted the signal could be located anywhere along one of the branches of a hyperbola passing between the two receivers that are foci points of that hyperbola. The intersection of two non-redundant hyperbola branches defines the location of the stroke at the open circle in the above figure (courtesy National Weather Service Training Center).

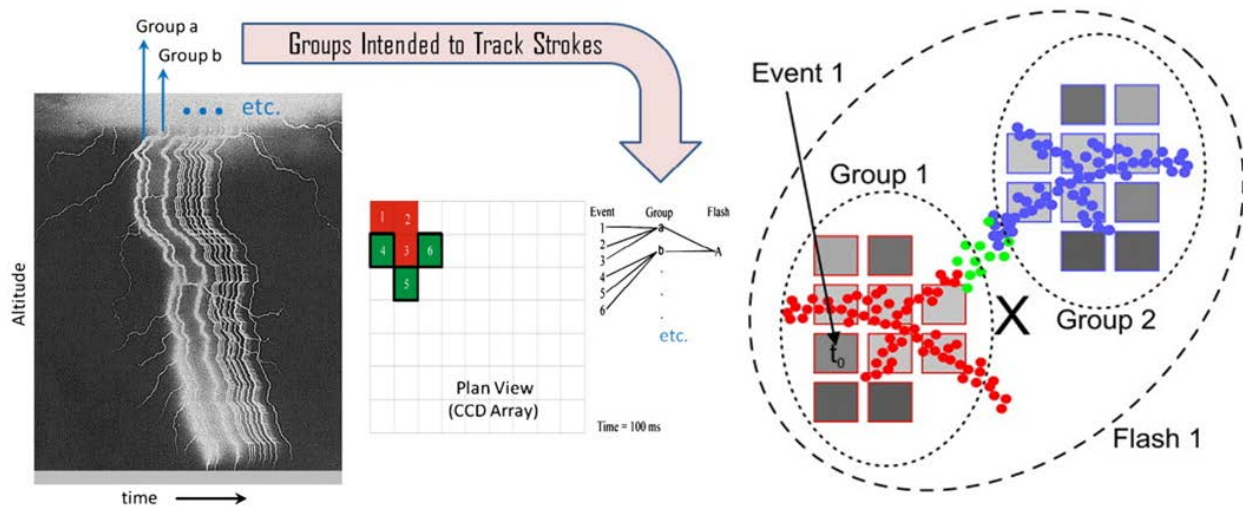
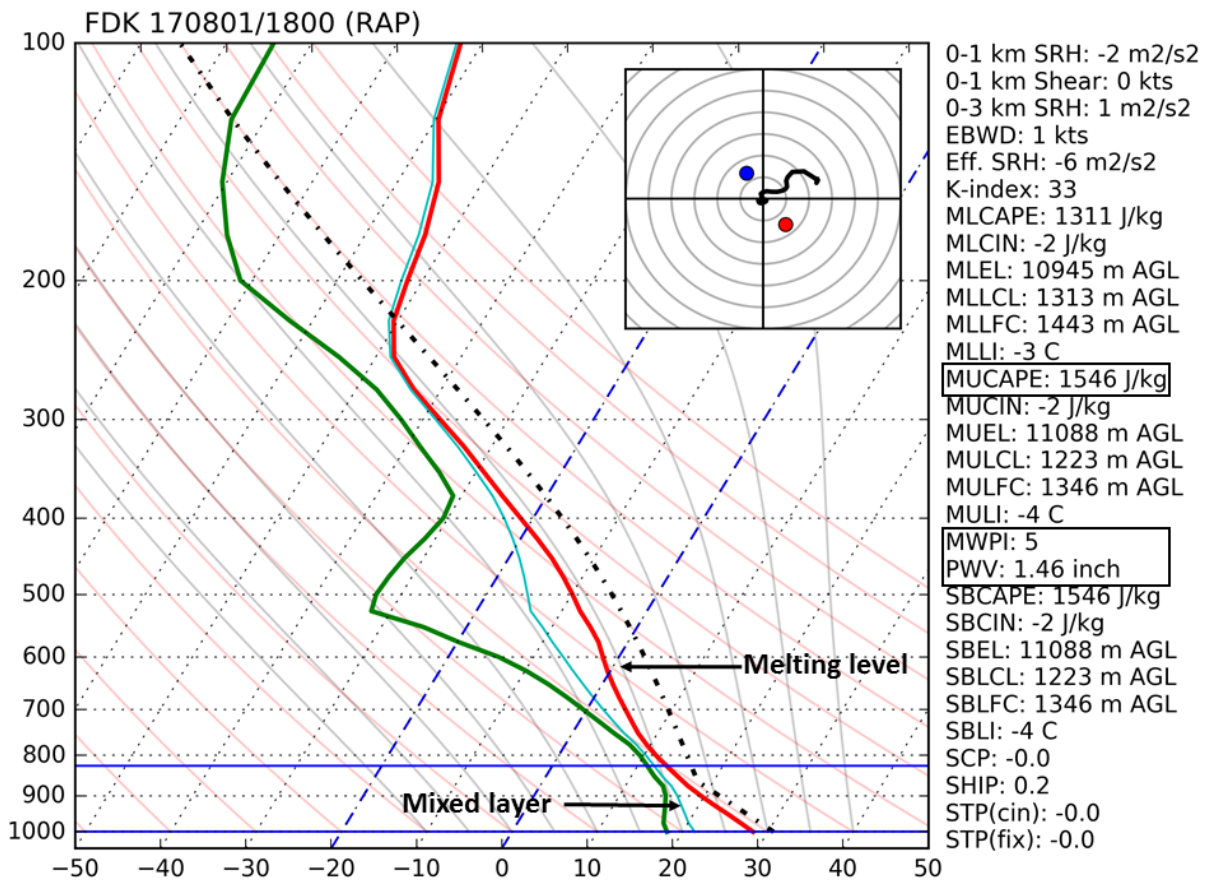


Figure 2. Graphical description of the Lightning Cluster Filter Algorithm (LCFA) in which optical groups track bright transient emissions from lightning (Goodman et al. 2013).



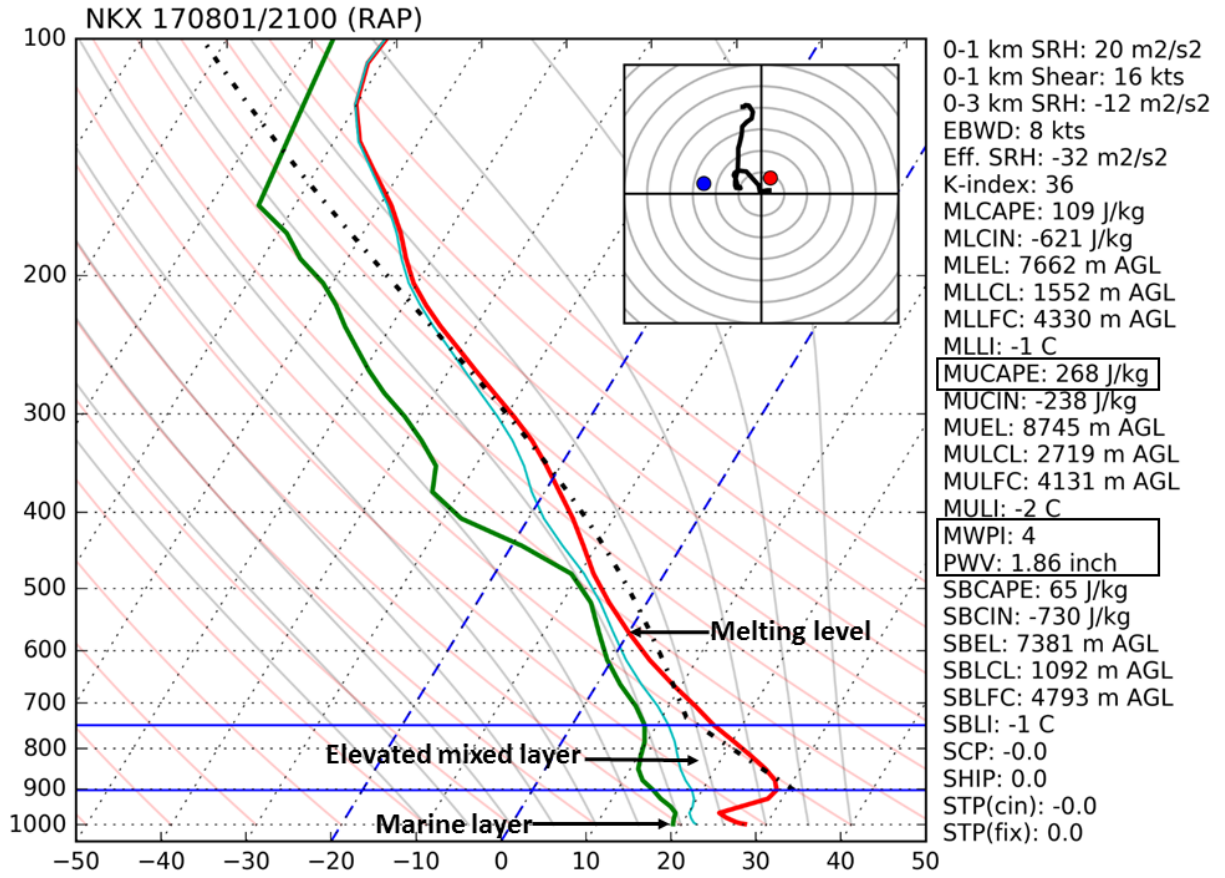


Figure 3. Rapid Refresh (RAP) model-derived thermodynamic profiles over Frederick, Maryland at 1800 UTC (top) and San Diego, California (bottom) at 2100 UTC 1 August 2017, respectively. The vertical axis is labeled in units of pressure (mb) and the horizontal axis is labeled in units of temperature ($^{\circ}$ C).

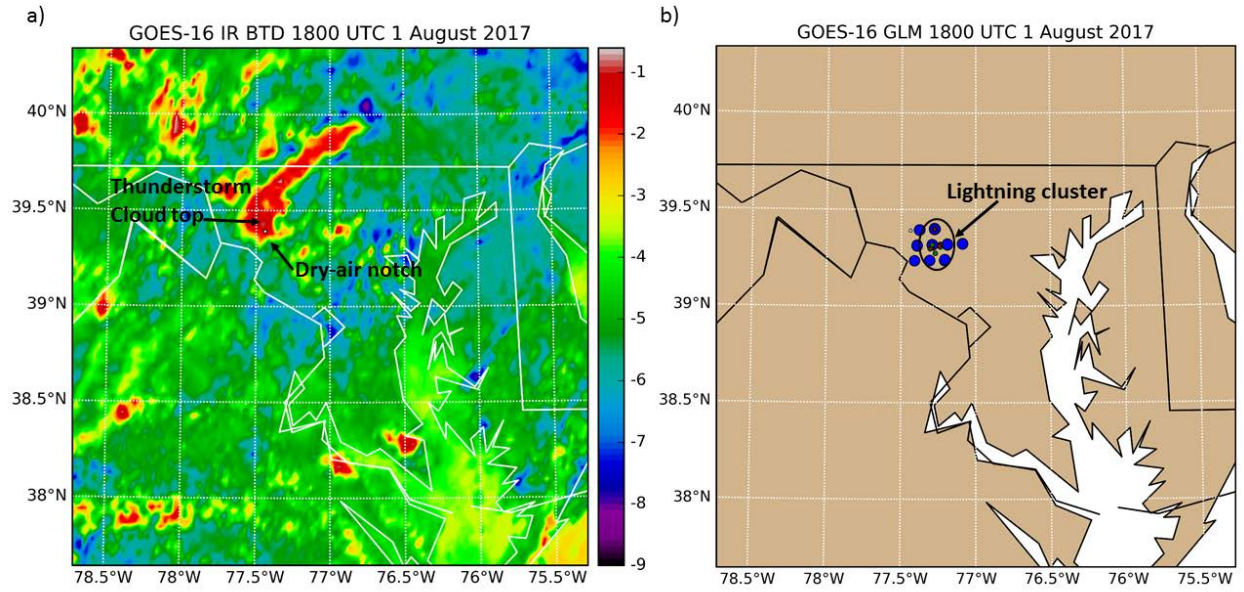


Figure 4. a) GOES-16 ABI Split-Window BT and b) GLM LFCA products at 1800 UTC 1 August 2017. White circle marks the location of downburst occurrence at Frederick, Maryland.

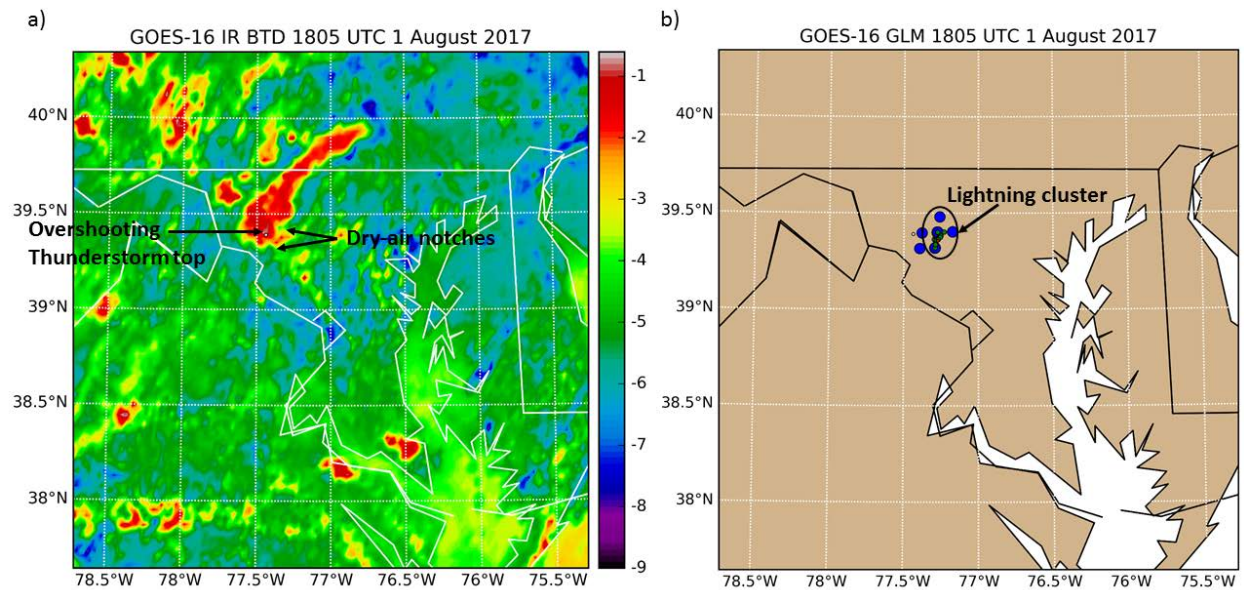


Figure 5. a) GOES-16 ABI Split-Window BT and b) GLM LFCA products at 1805 UTC 1 August 2017. White circle marks the location of downburst occurrence at Frederick, Maryland.

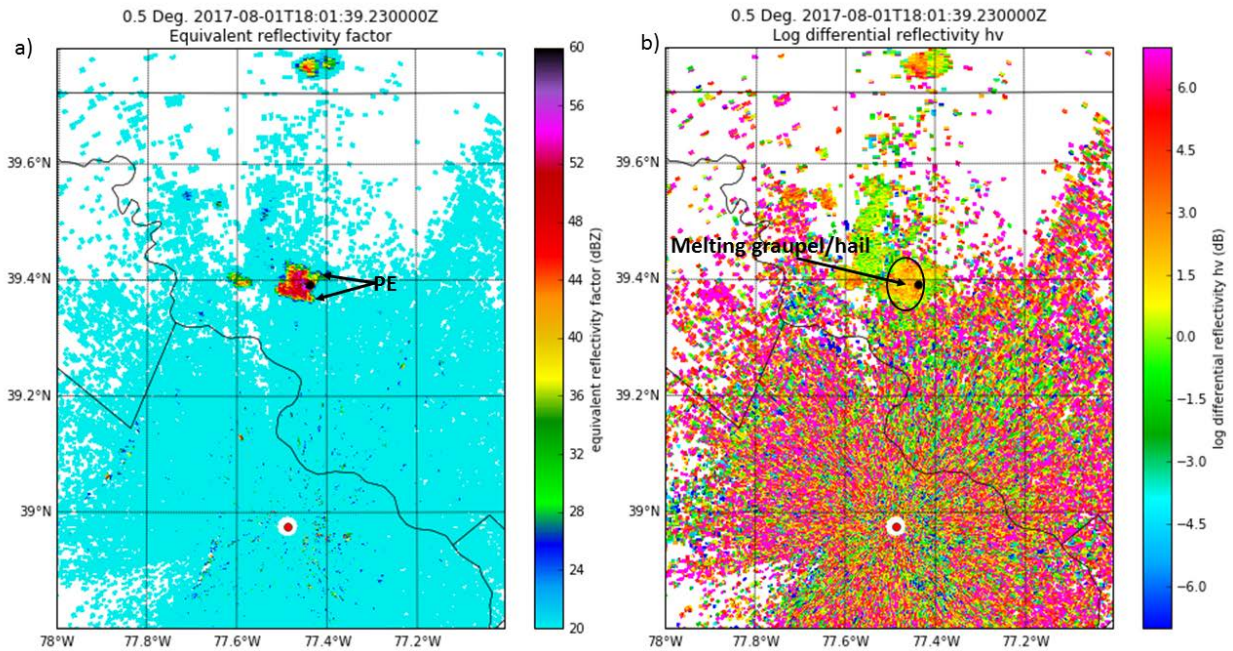


Figure 6. Sterling, Virginia NEXRAD a) reflectivity factor (dBZ) and b) differential reflectivity (dB) at 1801 UTC 1 August 2017. Black circle marks the location of downburst occurrence at Frederick, Maryland while “PE” indicates the location of associated protrusion echoes.

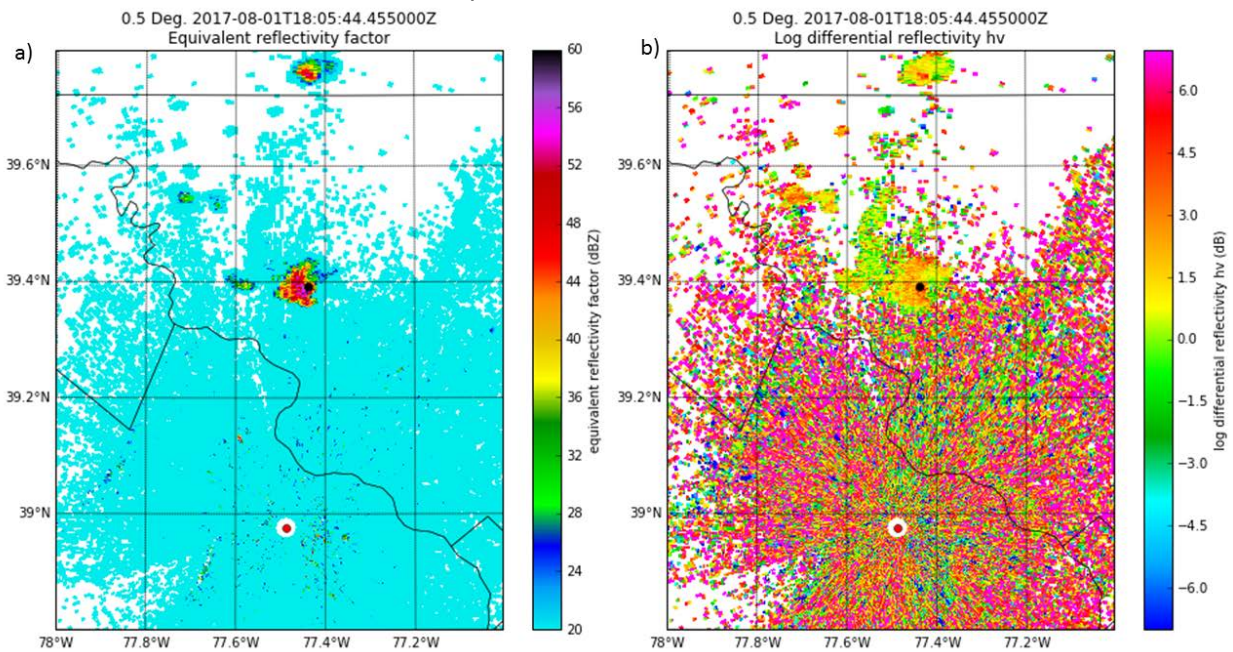


Figure 7. Sterling, Virginia NEXRAD a) reflectivity factor (dBZ) and b) differential reflectivity (dB) at 1805 UTC 1 August 2017. Black circle marks the location of downburst occurrence at Frederick, Maryland.

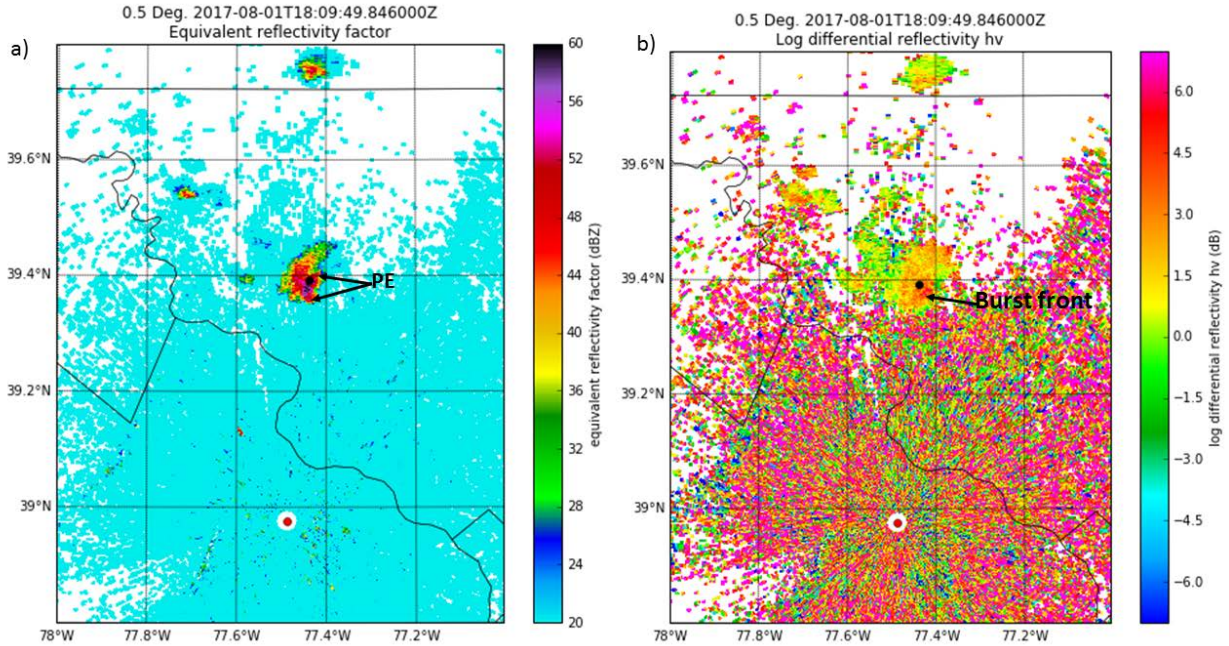


Figure 8. Sterling, Virginia NEXRAD a) reflectivity factor (dBZ) and b) differential reflectivity (dB) at 1809 UTC 1 August 2017. Black circle marks the location of downburst occurrence at Frederick, Maryland while “PE” indicates the location of protrusion echoes.

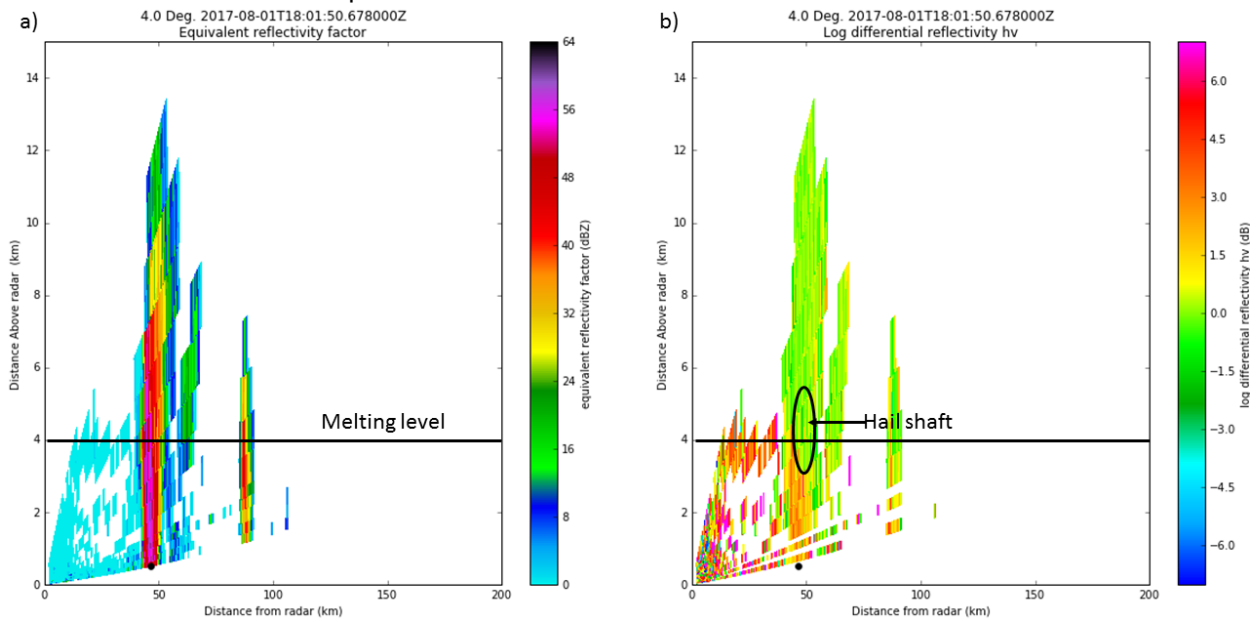


Figure 9. Sterling, Virginia NEXRAD cross sections of a) reflectivity and b) differential reflectivity at 1801 UTC 1 August 2017. Black circle marks the location of downburst occurrence at Frederick, Maryland. The presence of a descending hail shaft is a frequent precursor signature to microburst occurrence.

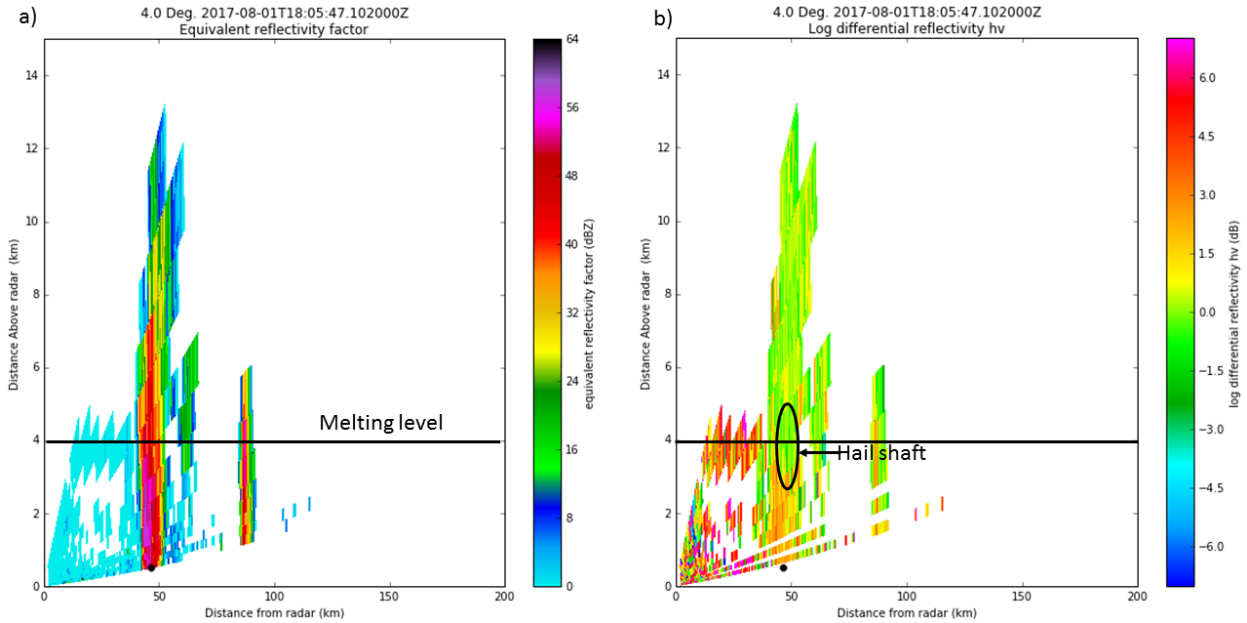


Figure 10. Sterling, Virginia NEXRAD cross sections of a) reflectivity and b) differential reflectivity at 1805 UTC 1 August 2017. Black circle marks the location of downburst occurrence at Frederick, Maryland.

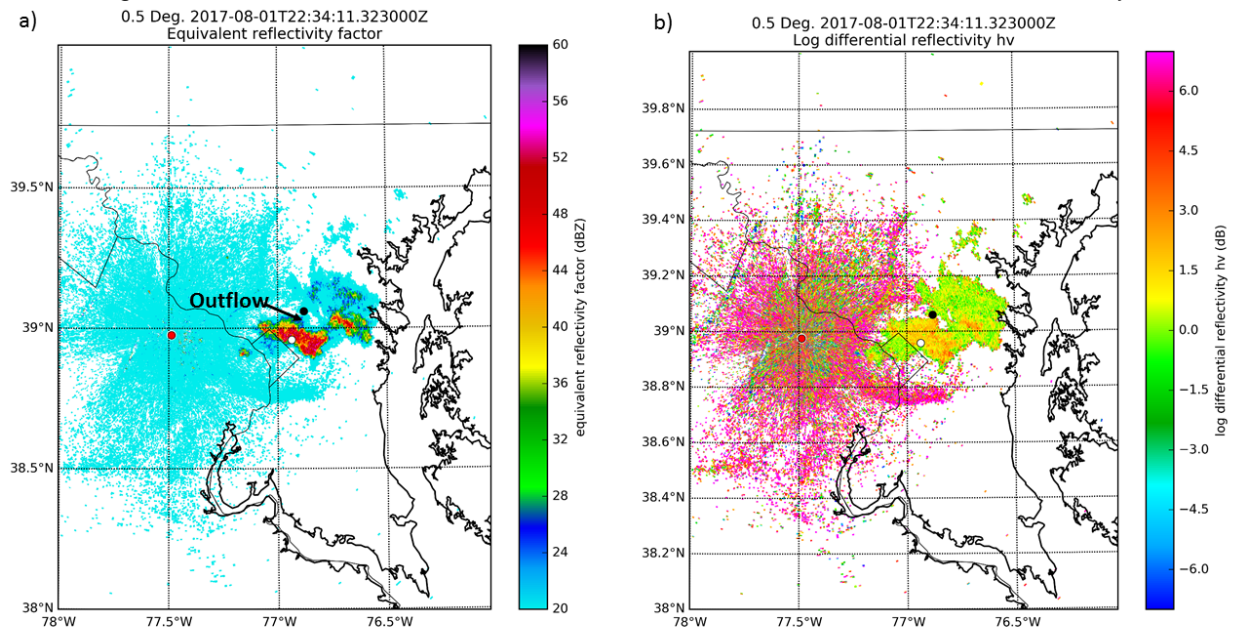


Figure 11. Sterling, Virginia NEXRAD a) reflectivity factor (dBZ) and b) differential reflectivity (dB) at 2234 UTC 1 August 2017. Black circle marks the location of the Beltsville, Maryland BLP, while white circle marks the location of downburst occurrence at Riverdale, Maryland.

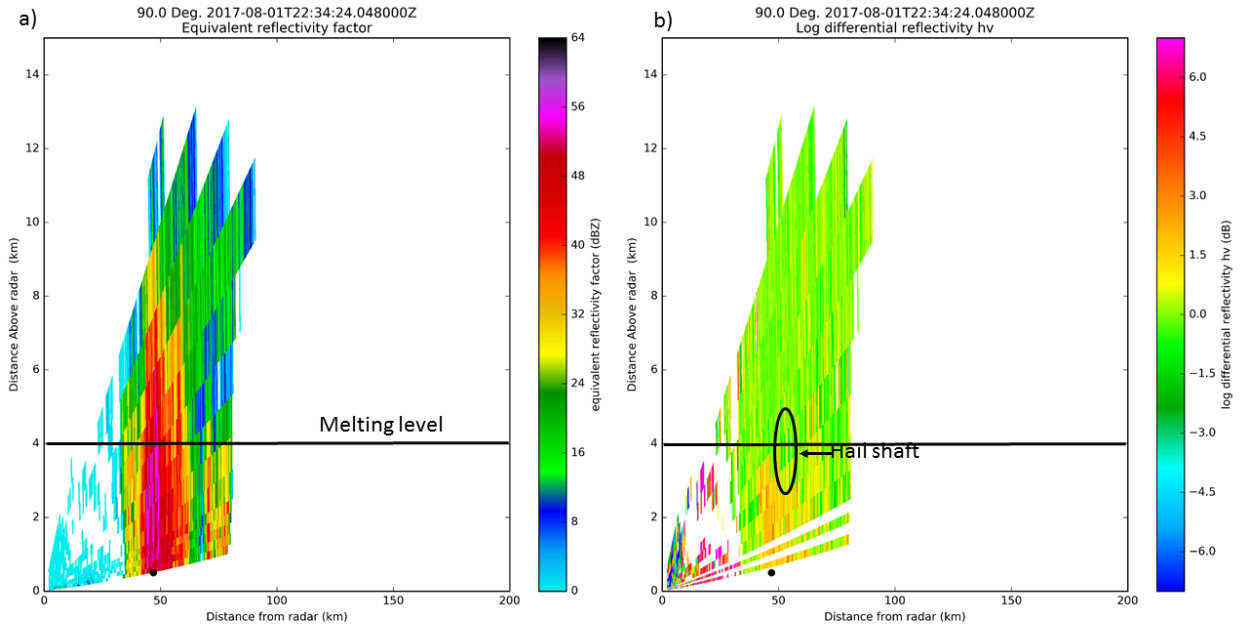


Figure 12. Sterling, Virginia NEXRAD cross sections of a) reflectivity and b) differential reflectivity at 2234 UTC 1 August 2017. Black circle marks the location of downburst occurrence at Riverdale, Maryland.



BLTMD Lat:39.06 Lon:-76.88 Elev:53m
RassTemperature| Mode:194m | Res:6min | QC:LEVEL 1 OR BETTER
WindSpeedDirection| Mode:194m | Res:6min | QC:LEVEL 1 OR BETTER
MARYLAND DEPARTMENT OF THE ENVIRONMENT

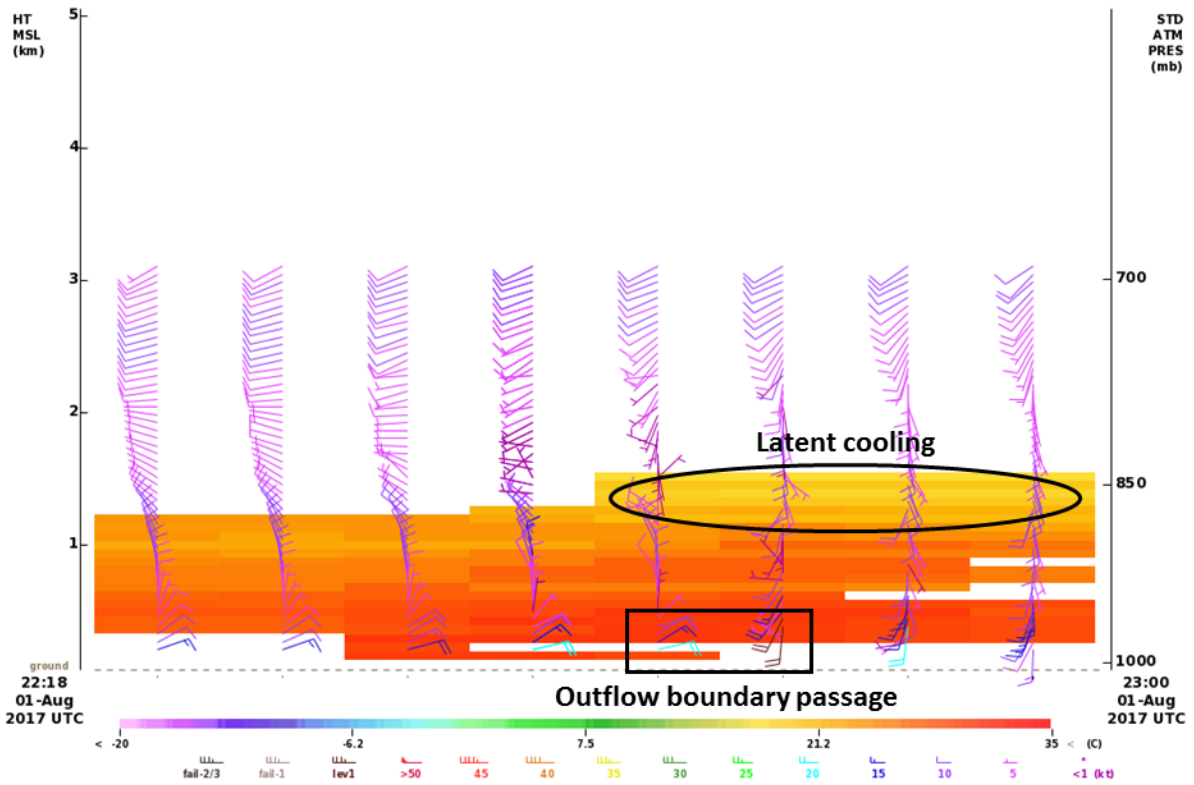


Figure 13. Time trend of vertical wind profiles over Beltsville, Maryland between 2218 and 2300 UTC 1 August 2017.

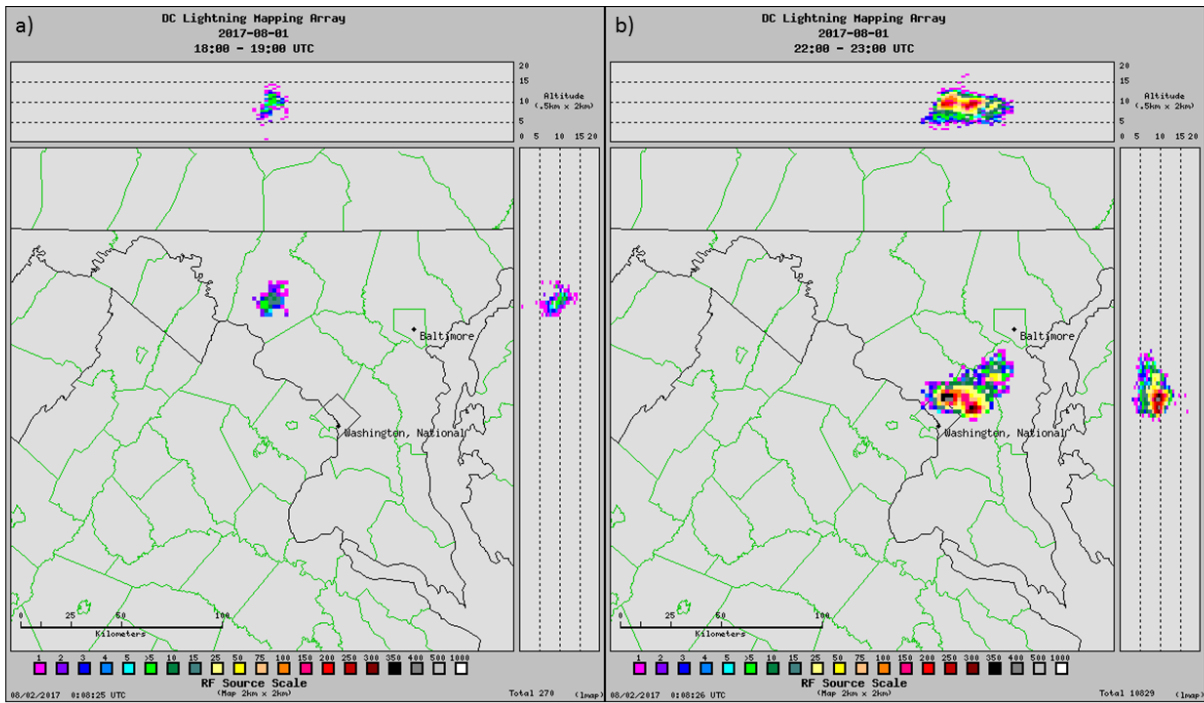


Figure 14. DCLMA radiofrequency (RF) source location images for a) 1800 to 1900 UTC and b) 2200 to 2300 UTC 1 August 2017.

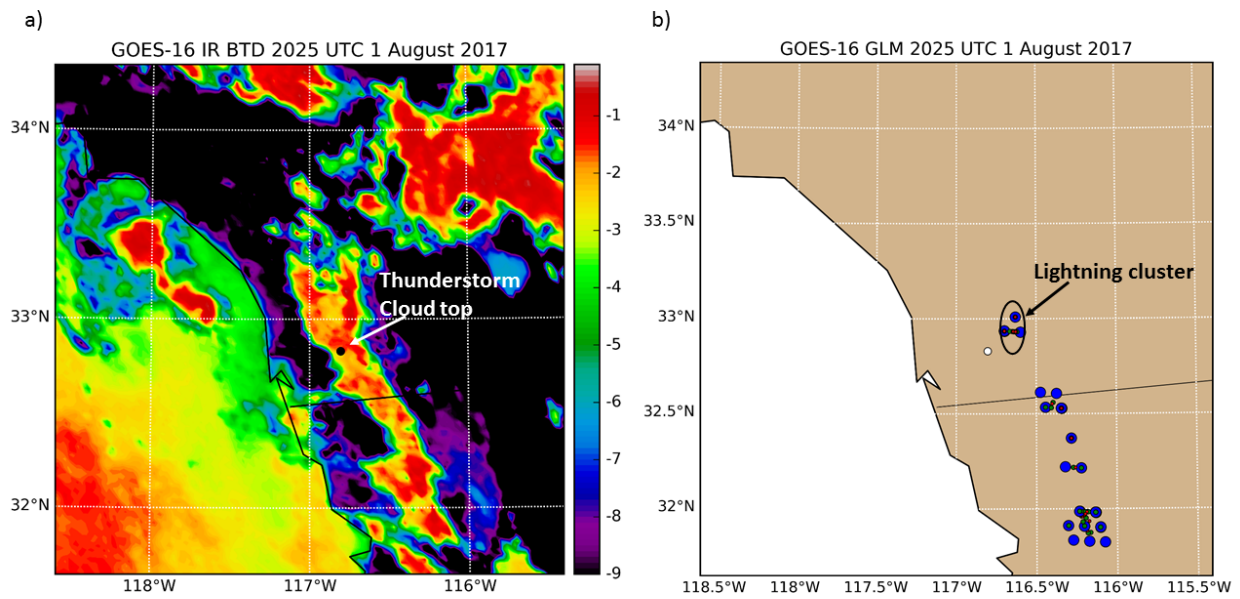


Figure 15. a) GOES-16 ABI Split-Window BTD and b) GLM LFCA products at 2025 UTC 1 August 2017. Black circle in a) and white circle in b) marks the location of downburst occurrence at Alpine, California.

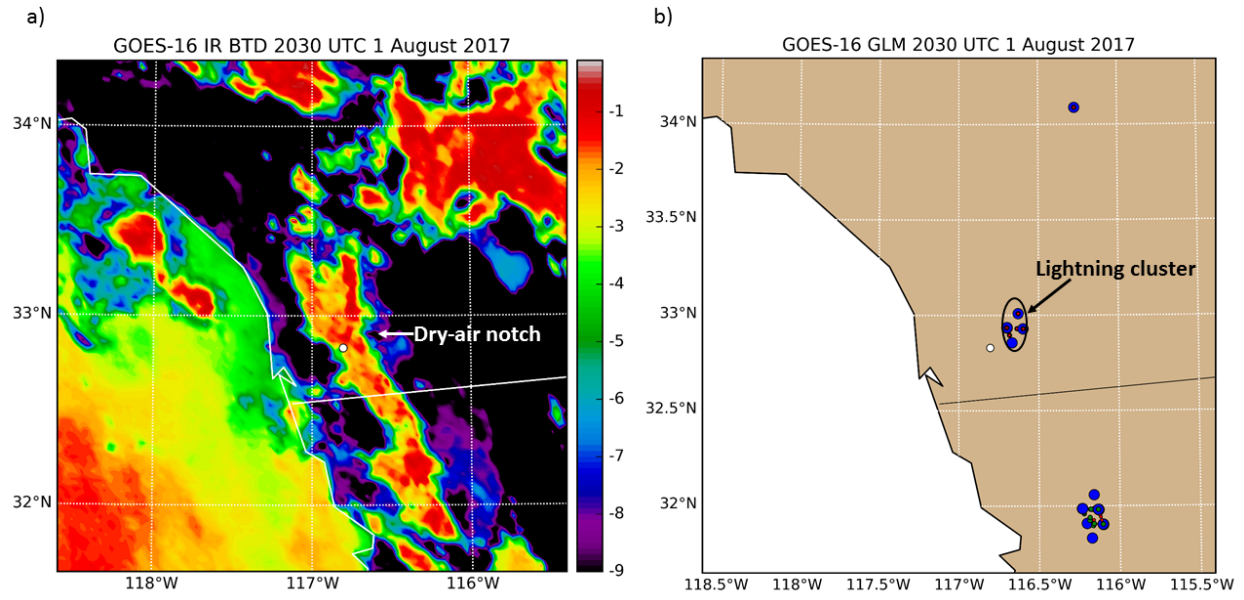


Figure 16. a) GOES-16 ABI Split-Window BT and b) GLM LFC products at 2030 UTC 1 August 2017. Black circle in a) and white circle in b) mark the location of downburst occurrence at Alpine, California.

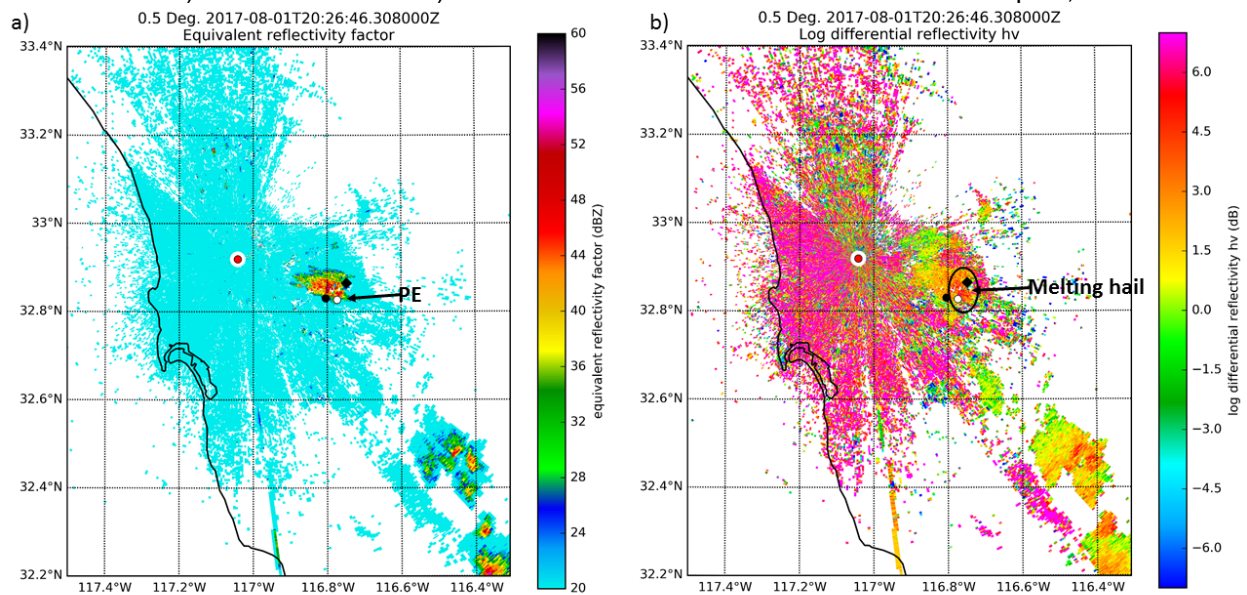


Figure 17. San Diego, California NEXRAD a) reflectivity factor (dBZ) and b) differential reflectivity (dB) at 2026 UTC 1 August 2017. Black and white circles mark the location of downburst wind occurrence in the Alpine, California area, while "PE" indicates the location of a protrusion echo.

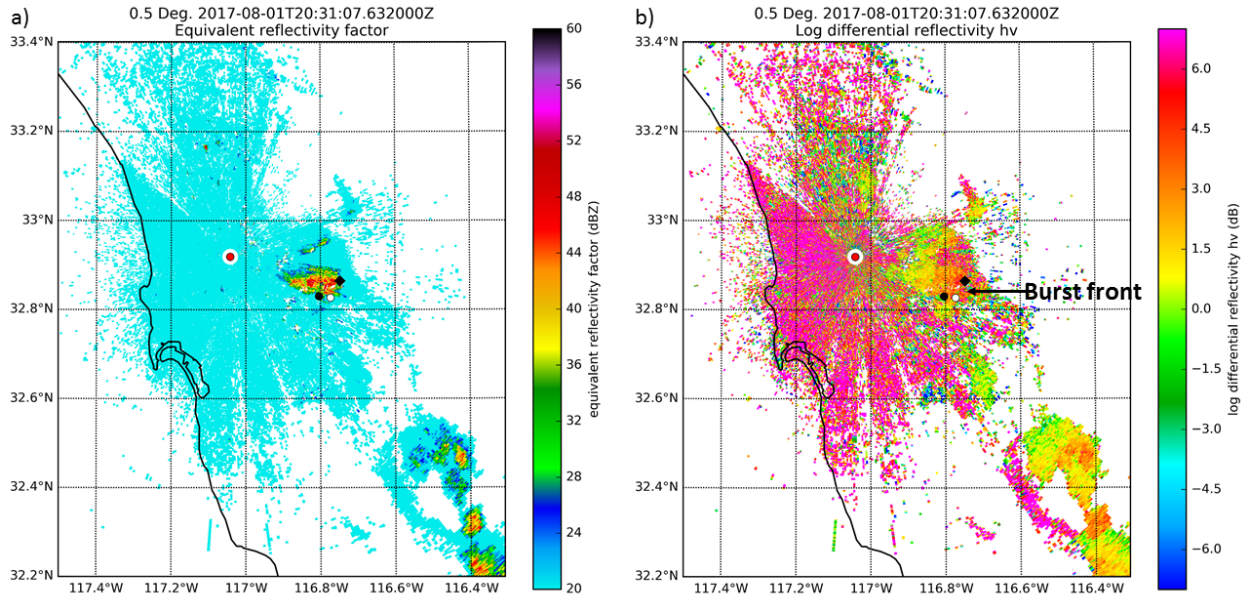


Figure 18. San Diego, California NEXRAD a) reflectivity factor (dBZ) and b) differential reflectivity (dB) at 2031 UTC 1 August 2017. Black and white circles mark the location of downburst wind occurrence in the Alpine, California area.

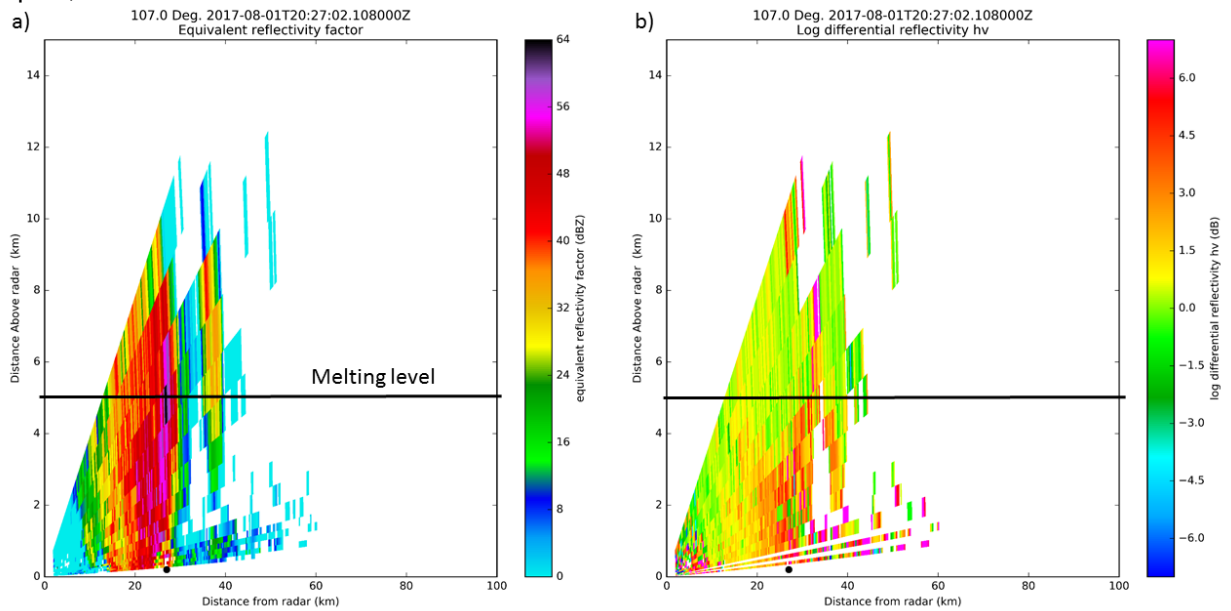


Figure 19. San Diego, California NEXRAD cross sections of a) reflectivity and b) differential reflectivity at 2027 UTC 1 August 2017. Black circle marks the location of downburst occurrence at Alpine, California.

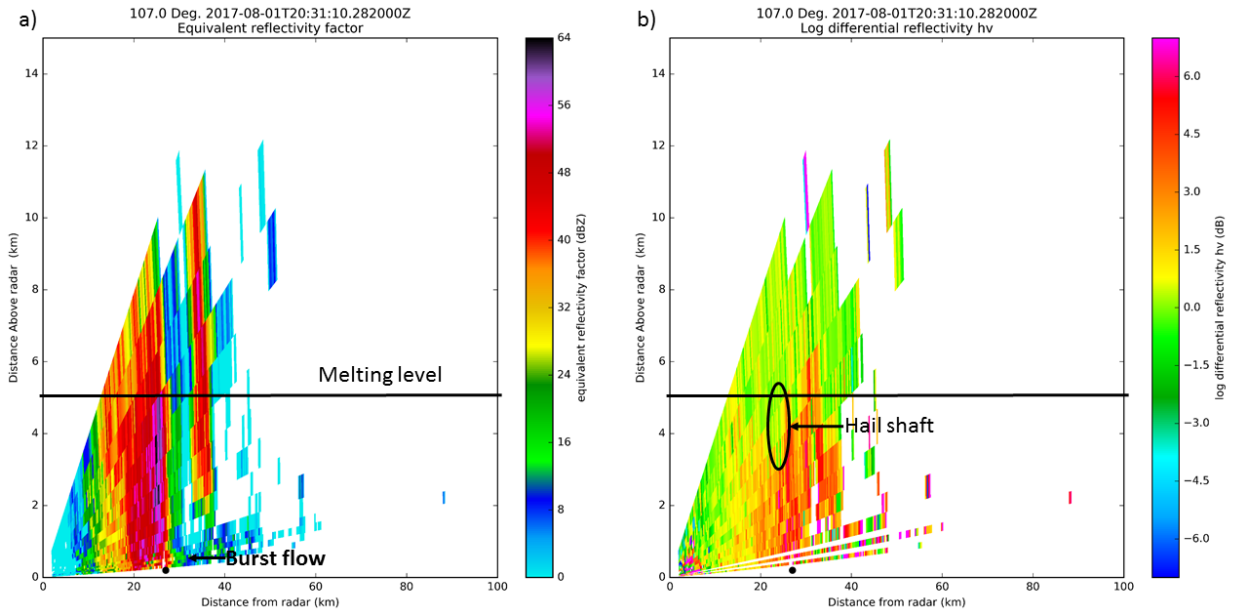


Figure 20. San Diego, California NEXRAD cross sections of a) reflectivity and b) differential reflectivity at 2031 UTC 1 August 2017. Black circle marks the location of downburst occurrence at Alpine, California.